Geophys. J. Int. (2003) **152,** 566–580

Effect of lateral viscosity variations in the top 300 km on the geoid and dynamic topography

O. Čadek[1] and L. Fleitout[2]

[1] *Department of Geophysics, Faculty of Mathematics and Physics, Charles University, V Holešovičkách* 2, 18000 *Prague, Czech Republic. E-mail: oc@karel.troja.mff.cuni.cz*

[2] *Laboratoire de Géophysique, Ecole Normale Supérieure,* 24 *rue Lhomond,* 75005 *Paris, France*

Accepted 2002 August 9. Received 2002 July 11; in original form 2001 November 9

SUMMARY

We have investigated the impact of lateral viscosity variations (LVV) in the top 300 km of the mantle on the long-wavelength gravitational response of the Earth. In contrast to the previous studies we demonstrate that the LVV may play a crucial role if a model with imposed plate velocities and partial layering is considered. Assuming LVV in the top mantle associated with the continental roots and the oceanic asthenosphere, we are able to explain a significant portion of the geoid (85 per cent) and of the free-air gravity data (55 per cent) without invoking a complex radial viscosity profile or assuming a lithosphere with an unrealistically low uniform viscosity. The best fit to the data is found for models in which mass anomalies located at the boundary between upper and lower mantles reduce the mass flux across the 660 km discontinuity by a factor of 3. These models are characterized by a low average value of viscosity in the asthenosphere below the oceans ($\sim 10^{19}$ Pa s) and a large viscosity contrast (>100) between the young suboceanic mantle and the deep continental roots. The viscosity in the deep upper mantle is found to be around 3×10^{20} Pa s while a value higher by at least two orders of magnitude is typical for the lower mantle. The predicted dynamic surface topography is influenced by the surface plate velocities and its amplitude amounts to a few hundred metres. Besides investigating the viscosity structures that reflect the different thicknesses of the lithosphere in continental and oceanic regions, we have searched for a large-scale pattern of lateral viscosity variation in the top 300 km that yields the best fit to the geoid. The pattern obtained by this inversion shows a good correlation with the ocean–continent distribution and 90 per cent of the geoid and 67 per cent of the free-air gravity can be explained.

Key words: asthenosphere, geoid, inversion, lateral heterogeneity, lithosphere, mantle viscosity.

1 INTRODUCTION

The present-day estimates of mantle viscosity are based on analyses of the response of a radially stratified mantle to surface and internal loading (Peltier 1989; King 1995a). Indeed, the lateral changes in viscosity were often found to affect very little the whole-mantle flow models with free-slip or a rigid upper boundary (Richards & Hager 1989; Ritzert & Jacoby 1992; Čadek *et al.* 1993; Colin 1993; Martinec *et al.* 1993; Zhang & Christensen 1993; Forte & Peltier 1994; King & Hager 1994). However, the actual flow conditions in the mantle are complex, falling somewhere in between the whole-mantle and fully layered situation. Furthermore, the mechanical effect of the stiff lithosphere, broken into several piecewise continuous plates, can be simulated by a no-slip condition with imposed plate velocities rather than by a free-slip condition (Karpychev & Fleitout 1996; Čadek & Fleitout 1999). The mantle flow driven by tectonic plates may induce a non-negligible dynamic topography that contributes to the total gravity response of the Earth. The amplitude of the gravity anomaly generated by the plate motion depends on the mechanical coupling between the lithospheric plates and the underlying mantle that is controlled by the laterally variable viscosity below the lithosphere (Ricard *et al.* 1988; Ravine & Phipps Morgan 1993; Karpychev & Fleitout 2000).

In the present paper we investigate the impact of lateral viscosity variations (LVV) in the top 300 km of the mantle on the gravitational response of the Earth using a flow model with partial layering and imposed plate velocities (Čadek & Fleitout 1999). The existence of large-scale lateral viscosity changes in the shallow mantle associated with the ocean–continent distribution has been suggested by a number of observations (Forsyth & Uyeda 1975; Ricard *et al.* 1991; Čadek & Ricard 1992; Karato & Wu 1993; Doin & Fleitout 1997). A subcontinental viscosity significantly higher than the viscosity below the oceans will be the starting point for the present study.

The effect of a laterally varying viscosity is investigated within the framework of internal loading theory and solved in the spectral domain. The formal description of the flow model including the lateral viscosity variations, partial layering and plate-velocity boundary condition is given in Section 2. Assuming that the viscosity pattern in the shallow mantle is dominated by viscosity variations between continental roots and the oceanic asthenosphere, we invert for the amplitude of the lateral viscosity contrast in the top 300 km, the radial changes in viscosity in a deeper mantle and the 'partial layering' providing the best fit to the geoid and gravity (Section 3.1). More complex viscosity models, including the deep continental roots and lateral viscosity variations in the oceanic asthenosphere, are examined in Sections 3.2 and 3.3. The assumption of the dominant role of the viscosity difference between the continental and oceanic regions is tested in Section 3.4 where the large-scale lateral viscosity structure in the asthenosphere providing the best fit to the geoid is derived by solving the inverse problem. In Section 4 we discuss the dynamic characteristics of the proposed model, namely the dynamic topography of the surface and of the 660 km discontinuity. The basic results and the main limitations of the model are discussed in Section 5. The present paper does not address the important issue of the lateral viscosity variations associated with the existence of lithospheric slabs in a deeper mantle. This problem, requiring an extremely high resolution, can hardly be solved by a spectral method and the application of a finite-element technique is more promising (Zhong & Davies 1999).

2 FORMALISM

2.1 Flow equations

The prediction of the long-wavelength non-hydrostatic geoid requires the solution of the Laplace–Poisson equation for gravitational potential to be combined with the computation of mantle flow (Hager & Clayton 1989; King 1995b). In the simplest case of a Newtonian, radially dependent viscosity, the appropriate equations can be classified according to order and degree and solved easily in the spectral domain (for more details see Ricard *et al.* 1984). In the case of any more complex rheology, the spectral equations are mutually coupled, which significantly complicates the solution. Since the coupling only affects the spectral form of the constitutive law we will now concentrate on the solution of the equations governing the flow in the mantle. The equations for the gravitational field are not affected by the lateral viscosity variations.

In a first approximation, the material forming the bulk of the mantle can be represented by a highly viscous incompressible Newtonian fluid. The equations governing the flow then read:

$$\nabla \cdot \boldsymbol{\sigma} + \rho \mathbf{g} = 0 \tag{1}$$

$$\nabla \cdot \mathbf{v} = 0 \tag{2}$$

$$\boldsymbol{\sigma} + p\boldsymbol{I} - \eta[\nabla \mathbf{v} + (\nabla \mathbf{v})^{\tau}] = 0, \tag{3}$$

where $\boldsymbol{\sigma}$ is the stress tensor, $\mathbf{g}$ is the gravity acceleration, ρ is the density, $\mathbf{v}$ is the velocity of flow, p is the pressure, $\boldsymbol{I}$ is the identity tensor, η is the Newtonian viscosity and τ denotes the transposition of a matrix. If the viscosity η is a general function of spherical coordinates r, θ and ϕ, the traditional degree-by-degree solution described, for example, by Ricard *et al.* (1984), fails since the spectral equations are mutually coupled through the non-linear term $\eta\nabla\mathbf{v}$ in eq. (3). There have been several attempts to adapt the spectral method for a fully 3-D viscosity case (Čadek *et al.* 1992, 1993; Colin 1993; Martinec *et al.* 1993; Zhang & Christensen 1993; Forte & Peltier 1994; D'Agostino *et al.* 1997; Martinec 1999; Tromp & Mitrovica 1999). In the present paper we follow the strategy based on the idea that the flow eqs (1)–(3) with a general 3-D viscosity can formally be converted to the usual 1-D problem by shifting all the coupling terms in eq. (3) to the right-hand side (Colin 1993; Zhang & Christensen 1993). The new equations can be solved iteratively with the aid of software developed for radially stratified viscosity models. For large lateral contrasts in viscosity the iterative scheme has to be stabilized by introducing a new variable $\mathbf{x} = \mathbf{v}\eta/\eta_0$, where η_0 is a radially dependent viscosity close to η. The equations can then be written in the following iterative form:

$$\nabla \cdot \boldsymbol{\sigma}^{n+1} + \rho \mathbf{g}^{n+1} = 0 \tag{4}$$

$$\nabla \cdot \mathbf{x}^{n+1} = \mathbf{x}^{n} \cdot \boldsymbol{\xi} \tag{5}$$

$$\boldsymbol{\sigma}^{n+1} + p^{n+1}\boldsymbol{I} - \eta_0[\nabla \mathbf{x}^{n+1} + (\nabla \mathbf{x}^{n+1})^{\tau}] = -\eta_0(\boldsymbol{\xi}\mathbf{x}^{n} + \mathbf{x}^{n}\boldsymbol{\xi}), \tag{6}$$

where n is the number of the iteration and $\boldsymbol{\xi} \equiv \nabla\,[\ln(\eta/\eta_0)]$. The corresponding spectral equations can be found in Colin (1993) and Zhang & Christensen (1993). Eqs (4)–(6) are formally the same as the equations governing the flow in a radially stratified mantle except for the two additional terms on the right-hand side, namely $\mathbf{x}^{n} \cdot \boldsymbol{\xi}$ and $\eta_0(\boldsymbol{\xi}\mathbf{x}^{n} + \mathbf{x}^{n}\boldsymbol{\xi})$. These two terms have to be recomputed at each iterative step and their evaluation takes most of the computation time. The products $\mathbf{x} \cdot \boldsymbol{\xi}$ and $\mathbf{x}\boldsymbol{\xi}$ are evaluated in the spatial domain in a grid of Gaussian points in θ and using the fast Fourier transform in ϕ (Martinec 1989). This method is sufficiently precise and less expensive than the use of analytical formulae for the products of spherical harmonic series.

The numerical solution of eqs (4)–(6) was carefully tested against the alternative methods based on a minimization of the dissipative energy (Čadek *et al.* 1992; Martinec *et al.* 1993). Further possibilities of testing were proposed by Zhang (1993). These tests prove that our code gives a correct and sufficiently precise solution. The iterative method gives a stable solution for lateral viscosity contrasts of at least 10^2–10^3 depending on the cut-off degree. The main advantage of the iterative method is its high speed, which allows both forward and inverse problems to be solved for viscosity structures with reasonable lateral contrasts. However, any spectral method becomes cumbersome if the viscosity structure shows large lateral gradients. Since large viscosity contrasts do indeed exist in the mantle, at least in its upper part, it is obvious that the iterative spectral code is a temporary tool suitable only for mantle flow models with a low resolution. For investigation of short-wavelength structures associated with large lateral viscosity contrasts the finite-approach approach is more suitable (Gasperini *et al.* 1991; Manga & O'Connell 1995; Zhong & Gurnis 1996; Zhong & Davies 1999; Kaufmann *et al.* 2000).

2.2 Boundary conditions

Following the previous inferences of viscosity from the geoid (Hager & Clayton 1989), we assume that the physical situation at the bottom boundary ($r = 3480$ km) is reasonably well approximated by the free-slip boundary conditions:

$$v_r = 0 \tag{7}$$

$$\sigma_{r\theta} = \sigma_{r\phi} = 0. \tag{8}$$

The same boundary conditions have also often been used for the top boundary (Hager & Clayton 1989; Forte *et al.* 1993; King 1995b;

Thoraval *et al.* 1995; Kido & Čadek 1997; Le Stunff & Ricard 1997). However, the free-slip surface models cannot provide a good fit to the observed plate velocity unless strong lateral variations in viscosity are imposed in the top of the mantle (Karpychev & Fleitout 1996; Zhong & Gurnis 1996). There have been several attempts at including a complex rheology of the lithosphere into the framework of internal loading theory (Wen & Anderson 1997; Zhong & Davies 1999). This type of modelling, however, requires a high spatial resolution and is rather expensive, in particular if an inverse problem is to be solved. Moreover, one does not know what is the appropriate plate boundary rheology. To avoid the problems with the rheological description of the plate boundaries some authors have attempted to mimic the plate-like behaviour of the lithosphere by including the geometry of plates in the models with a radially stratified mantle (Ricard & Vigny 1989; Ricard & Bai 1991; Corrieu *et al.* 1994) and by solving for the force balance for each plate predicted by the large-scale global flow computation. As explained in Čadek & Fleitout (1999), this approach may be misleading since it does not properly quantify the complex effects of plate boundary resistive forces and short-wavelength slab pull. As shown by Karpychev & Fleitout (1996), one must be able to describe what occurs on a scale of a few tens of kilometres near the plate boundary in order to quantify correctly the force balance of a plate. Since the strength of the plate boundaries is presently unknown the simplest way to include the plate-like behaviour of the lithosphere is to impose directly the observed plate velocities on the top of the mantle. The plate-velocity boundary condition was used already in the first attempts to study the relationship between the plate motion and mantle flow (Hager & O'Connell 1979, 1981). This approach yields no information on the relative balance between plate boundary forces and driving forces from the internal load but presents no inconvenience concerning the geoid computation (for a more detailed discussion of this topic see Karpychev & Fleitout 1996 and Čadek & Fleitout 1999).

In the present paper, the set of eqs (1)–(3) is solved in a spherical shell with the top boundary located at a depth of 80 km. The boundary condition prescribed at this surface is formulated in terms of the observed plate velocities. Both radial and lateral components of velocity are considered:

$$\mathbf{v} = h\mathbf{e}_r \nabla \cdot \mathbf{u} + \mathbf{u}, \tag{9}$$

where h is the thickness of the lithospheric layer above the boundary ($h = 80$ km), $\mathbf{e}_r$ is the unit radial vector and $\mathbf{u}$ is the velocity of the observed plate motion. The radial deformation of the 80 km thick layer above the boundary is evaluated in the same way as in the study by Čadek & Fleitout (1999): by solving the set of eqs (1)–(3) with boundary conditions (7)–(9) we evaluate the vertical and tangential stress acting at the base of the lithosphere. The value of these stresses is then used to compute the corresponding 'surface topography'. This computation is carried out on the assumption that the lithosphere behaves as a perfect membrane with a free-slip outer boundary (Ribe 1992). The effect of the self-gravitation arising from the lithospheric deformation is included.

In distinction with the case including the free-slip boundary condition, the dynamic geoid obtained for the flow model with imposed plate velocities is sensitive to both the relative changes and the absolute value of the viscosity (Ricard *et al.* 1984, 1988). The dynamic geoid $G(\rho, \eta)$ corresponding to a viscosity distribution η and a density ρ is a superposition of the geoid $G^{pm}(0, \eta)$ generated by the plate motion boundary condition (proportional to the absolute value of the viscosity) and the geoid $G^{ns}(\rho, \eta)$ obtained for the density distribution ρ and a no-slip upper boundary (independent of the absolute value of the viscosity, though varying with the radial and lateral viscosity contrasts). The amplitude of the geoid depends on the density ρ and the viscosity η linearly:

$$G(\alpha\rho, \beta\eta) = \alpha G^{ns}(\rho, \eta) + \beta G^{pm}(0, \eta), \tag{10}$$

where α and β are real numbers. As demonstrated by Karpychev & Fleitout (1996) in a 2-D self-consistent model, the effect of the plate motion on the geoid and dynamic topography may be significant provided that the viscosity of the mantle is sufficiently high. If the viscosity in the lower mantle is higher than in the upper mantle, the topography and the geoid induced by the plate motion have signs opposite to those usually expected for free-slip boundary models: the topographic and geoid elevations are located above the subduction zones while the divergent plate boundaries are associated with topographic and geoid depressions.

Finally, we rewrite the boundary conditions (7)–(9) to a form a suitable iterative solution of eqs (4)–(6):

$$x_r^{n+1} = 0 \tag{11}$$

$$\sigma_{r\theta}^{n+1} = \sigma_{r\phi}^{n+1} = 0 \tag{12}$$

$$\mathbf{x}^{n+1} = \frac{\eta}{\eta_0}(h\mathbf{e}_r \nabla \cdot \mathbf{u} + \mathbf{u}). \tag{13}$$

2.3 Partial layering

Various processes may hamper the flow across the 660 km discontinuity (Ringwood 1990; Solomatov & Stevenson 1994; Le Stunff & Ricard 1997). The total resistive effect of these processes is a complex non-linear function of state parameters, chemical composition, velocity of flow and other quantities (Christensen 1998). Since this function is not yet satisfactorily known, the resistive forces acting at the 660 km discontinuity have to be represented in a simplified way (Le Stunff & Ricard 1997).

In the present paper, we follow the strategy proposed by Čadek & Fleitout (1999) who introduced a formal parameter λ characterizing the portion of the layered flow in mantle circulation. If $\mathcal{M}^{\mathrm{LF}}$ and $\mathcal{M}^{\mathrm{WMF}}$ are, respectively, the layered and whole-mantle flow models obtained by solving eqs (1)–(3) and (7)–(9), then, using the layering coefficient λ, $0 \le \lambda \le 1$, a partially layered model $\mathcal{M}_\lambda^{\mathrm{PLF}}$ can be defined as follows:

$$\mathcal{M}_\lambda^{\mathrm{PLF}} = (1-\lambda)\mathcal{M}^{\mathrm{WMF}} + \lambda\mathcal{M}^{\mathrm{LF}}. \tag{14}$$

It can be shown that for a given density ρ and viscosity η the layering coefficient λ corresponds to a surface load imposed at a depth of 660 km (for details see Čadek & Fleitout 1999). Rewriting eq. (14) for the radial velocity at a depth of 660 km and using the fact that v_r^{LF} vanishes at the boundary between the upper and lower mantle we obtain

$$v_r^{\mathrm{PLF}} = (1-\lambda)v_r^{\mathrm{WMF}}. \tag{15}$$

Eq. (15) clarifies the physical meaning of the parameter λ: it characterizes the reduction of the mass exchange across the 660 km discontinuity with respect to the whole-mantle flow.

2.4 Parametrization

In the simplest case discussed in Section 3.1, we introduce six free parameters that fully define our dynamic model of the mantle. Three of them, η_{UM}, η_{LM} and $\eta_{\mathrm{C/O}}$, characterize the viscosity structure of the mantle (for more details see Section 3.1), another two, c_{UM} and c_{LM}, determine the amplitudes of density heterogeneities $\delta\rho$

deduced from a tomographic model of relative seismic anomalies $\delta V/V$,

$$\delta\rho/\rho = c\delta V/V \tag{16}$$

and the final one is the layering coefficient λ defined in Section 2.3. The distribution of seismic anomalies $\delta V/V$ is taken from the shear wave tomographic model of Woodhouse and Trampert (Woodhouse & Trampert 1995; J. Trampert, *pers. comm.* 1997). We also tested other long-wavelength models (Su *et al.* 1994; Masters *et al.* 1996) and we obtained basically the same results (*cf.* Čadek & Fleitout 1999). The use of recent high-resolution tomographic models (e.g. van der Hilst *et al.* 1997) led to somewhat worse results: the very high resolution in these models is probably achieved at the expense of the low-degree part of the spectrum.

In this study we ignore the density anomalies in the top 300 km of the mantle because they cannot be properly estimated on the basis of a seismic tomographic model (Doin *et al.* 1996). Since the velocity-to-density scaling is often found to be close to zero or negative in the transition zone (Čadek & Fleitout 1999) we also test a density model derived from the present-day location of slabs in the upper mantle. The scaling factor $c_{\rm UM}$ is then replaced by a parameter χ optimizing the amplitude of the slab densities,

$$\delta\rho = \chi\rho_{\rm slab}, \tag{17}$$

where $\rho_{\rm slab} = 0.080$ g cm^{-3} for slabs older than 90 Myr and 0.080 g cm^{-3} $\times \sqrt{(\text{age}/90\,\text{Myr})}$ for younger slabs (Lithgow-Bertelloni & Richards 1998). In contrast to some other studies, the slab model is only used for the upper mantle, while the lower-mantle density structure is always deduced from the seismic tomographic model mentioned above.

2.5 Inversion

The inverse problem is formulated in the usual way, as a search for the values of the model parameters $\eta_{\rm UM}$, $\eta_{\rm LM}$, $\eta_{\rm C/O}$, $c_{\rm UM}$ (or χ), $c_{\rm LM}$ and λ that yield the best fit to the observed long-wavelength geoid or free-air gravity in the sense of an L^2 norm (King 1995b; Čadek & Fleitout 1999). The geoid-fitting function is mainly sensitive to the lowest degrees of the gravitational field, in particular to degree two. To employ the gravitational signal at higher degrees we also test the free-air gravity anomalies (Peltier *et al.* 1992; Forte *et al.* 1994). The agreement between the predicted and observed quantities will be expressed as a percentage of the fitted data, or the variance reduction P,

$$P = \left[1 - \frac{\sum_{\ell=2}^{8}\sum_{m=-\ell}^{\ell}\left(G_{\ell m}^{\rm obs} - G_{\ell m}^{\rm pred}\right)^2}{\sum_{\ell=2}^{8}\sum_{m=-\ell}^{\ell}\left(G_{\ell m}^{\rm obs}\right)^2}\right] \times 100\,\text{per cent}, \tag{18}$$

where $G_{\ell m}^{\rm obs}$ is the spherical harmonic coefficient of the observed quantity, namely of the geoid or the free-air gravity, and $G_{\ell m}^{\rm pred}$ is the spherical harmonic coefficient predicted for a given set of model parameters. The observed gravitational signal was corrected for the lithospheric effects (Doin *et al.* 1996). A relatively low value of the cut-off degree in the variance reduction formula ($\ell_{\rm max} = 8$) is in agreement with the results presented by Le Stunff & Ricard (1995) who showed that a substantial portion of the geoid at degrees $\ell \geq 10$ can be explained by static effects of the lithospheric mass anomalies.

Quantities η, ρ and $\mathbf{u}$ in eqs (4)–(6) and (11)–(13) are truncated at degree 12–24 and the solution ($\mathbf{x}$, $\boldsymbol{\sigma}$) is determined up to degree 24–48, depending on the imposed lateral viscosity contrast.

The maximum of the function $P(\eta_{\rm UM}, \eta_{\rm LM}, \eta_{\rm C/O}, c_{\rm UM}$ or $\chi, c_{\rm LM}, \lambda)$ is found by a systematic exploration of the model space. The results of the inversions will be shown with the aid of 2-D maps, constructed as projections of function P to appropriate model subspaces (Thoraval & Richards 1997). Although this visualization method does not give full information concerning the function P, it allows the trade-off between individual model parameters to be easily recognized.

3 3-D VISCOSITY MODELS

3.1 Basic model

As a first step, we will investigate the effect of a decrease of viscosity in the mantle below the oceans (viscosity structure I, Fig. 1a). The characteristic function of the continents is adopted from the model 3SMAC by Nataf & Ricard (1996). The viscosity structure of the mantle is characterized by three parameters $\eta_{\rm UM}$, $\eta_{\rm LM}$ and $\eta_{\rm C/O} \equiv \eta_{\rm UM}/\eta_{\rm ocean}$ (Fig. 2), explored in the following ranges: $10^{19} \leq \eta_{\rm UM} \leq 10^{22}$ Pa s, $1 \leq \eta_{\rm LM}/\eta_{\rm UM} \leq 10^4$ and $1 \leq \eta_{\rm C/O} \leq 200$. The upper bound for the parameter $\eta_{\rm C/O}$ corresponds to a limiting value of the viscosity contrast for which the iterative equations given in Section 2.1 can be solved without large computational expense and numerical difficulties. The thickness of the asthenospheric channel considered below the oceans is derived from the depth variations of the amplitude of seismic anisotropy (Montagner & Tanimoto 1991), which shows a significant decrease at a depth between 250 and 300 km.

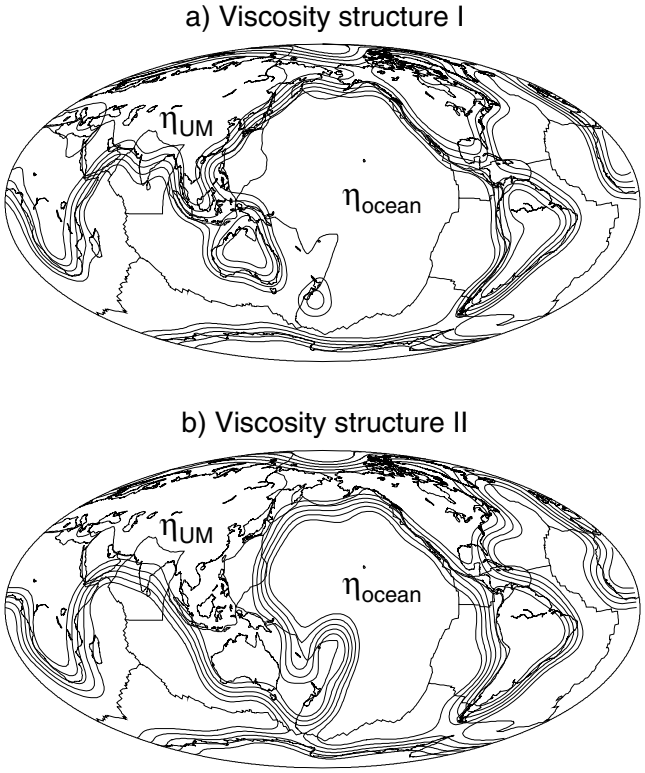

Figure 1. (a) Lateral viscosity structure in the top part of the mantle considered in Section 3.1. While the viscosity below the oceans drops to a value of $\eta_{\rm ocean}$ the viscosity below the continents ($\eta_{\rm UM}$) is constant throughout the upper mantle. The viscosity structure is plotted in a logarithmic scale. The isoline interval is 0.2 $\log_{10}(\eta_{\rm UM}/\eta_{\rm ocean})$. (b) The same as in (a) but with subduction zones included in regions of higher-than-average viscosity. The depth dependence of viscosity is illustrated in Fig. 2.

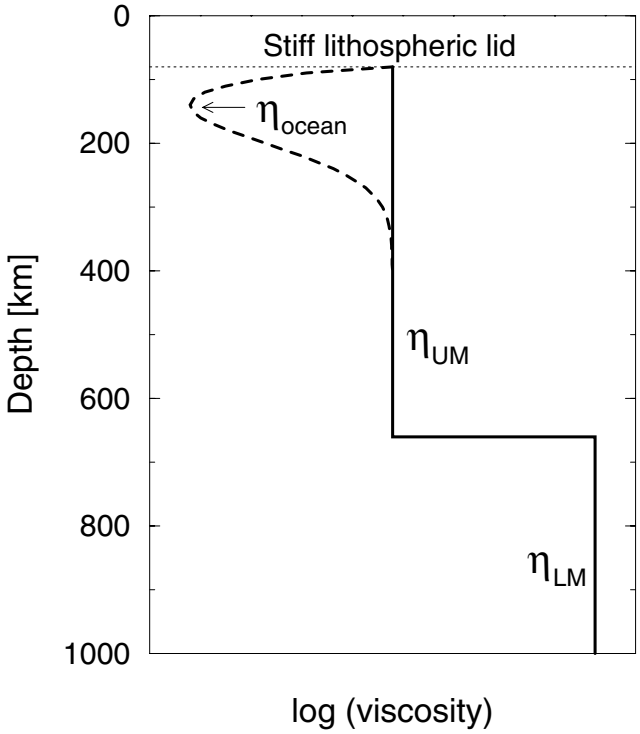

Figure 2. Viscosity as a function of depth below the oceans (dashed line) and the continents (solid line). The lower-mantle viscosity η_{LM} does not vary with depth.

The maximum percentage of the data predicted for models without LVV is 42 per cent for gravity and 76 per cent for the geoid. The inclusion of a low-viscosity channel below the oceans (structure I, Fig. 1a) leads to a slightly better fit to gravity (46 per cent) but gives basically no improvement for the geoid prediction. A significantly larger percentage of the gravitational signal (50 per cent of gravity and 83 per cent of the geoid) can be predicted if the subduction zones are included in regions of higher-than-average viscosity (viscosity structure II, Fig. 1b). The viscosity structures I and II differ significantly only in the South-West Pacific where the viscosity model II shows a high viscosity. Although the area of this high-viscosity region is rather small it plays an important role in predicting the gravitational signal because it coincides with a region of high plate convergence.

We will now discuss the results obtained for the viscosity structure II in detail. In Fig. 3 the maximum value of the variance reduction P, eq. (18), is plotted as a function of viscosity contrast $\eta_{C/O}$ and of other three variables, η_{UM}, η_{LM}/η_{UM} and λ. The top, middle and bottom panels show, respectively, the functions

$$P_{top}(\eta_{C/O}, \eta_{UM}) \equiv \max_{\eta_{LM}, c_{UM}, \chi, c_{LM}, \lambda} P(\eta_{UM}, \eta_{LM}, \eta_{C/O}, c_{UM} \text{ or } \chi, c_{LM}, \lambda) \quad (19)$$

$$P_{mid}(\eta_{C/O}, \eta_{LM}/\eta_{UM}) \equiv \max_{\eta_{UM}, c_{UM}, \chi, c_{LM}, \lambda} P(\eta_{UM}, \eta_{LM}/\eta_{UM}, \eta_{C/O}, c_{UM} \text{ or } \chi, c_{LM}, \lambda) \quad (20)$$

$$P_{bot}(\eta_{C/O}, \lambda) \equiv \max_{\eta_{UM}, \eta_{LM}, c_{UM}, \chi, c_{LM}} P(\eta_{UM}, \eta_{LM}, \eta_{C/O}, c_{UM} \text{or } \chi, c_{LM}, \lambda). \quad (21)$$

The percentage of the predicted geoid is given on the left while the panels on the right illustrate the prediction for free-air gravity. The best fit to the geoid (>80 per cent) is found for $\eta_{C/O} > 30$, $\lambda \sim 0.7$, $\eta_{LM}/\eta_{UM} \geq 100$ and $\eta_{UM} \leq 8 \times 10^{20}$ Pa s. The best-fitting models are thus characterized by a pronounced asthenosphere in the oceanic regions ($\eta_{ocean} \leq 3 \times 10^{19}$ Pa s) and rather high values of viscosity in the lower mantle ($\eta_{LM} > 5 \times 10^{22}$ Pa s). The values of λ, η_{UM} and η_{LM} inferred from the geoid in the present study do not differ much from the model obtained by Čadek & Fleitout (1999) on the assumption of a radially stratified mantle. Note, however, that the geoid predicted without the lateral viscosity changes ($\eta_{C/O} = 1$) can reproduce only 68 per cent of the data unless $\eta_{UM} < 10^{20}$ Pa s (Fig. 4). The model parameters inferred from the free-air gravity are rather similar to those obtained for the geoid. The best fit (∼50 per cent) to the gravity data is obtained for $\lambda \sim 0.65$, $\eta_{C/O} \sim 50$, $\eta_{UM} = 3 \times 10^{20}$ Pa s and $\eta_{LM} \sim 5 \times 10^{22}$ Pa s. The values of the parameters λ, $\eta_{C/O}$ and η_{LM} that best satisfy the gravity are somewhat lower than those which fit the geoid. On the other hand, the geoid can be well predicted even for rather low values of the upper-mantle viscosity ($\eta_{UM} \sim 10^{19}$ Pa s) which, however, do not give a reasonable fit to the gravity and have therefore to be excluded.

Our estimate of η_{ocean} is consistent with the value of viscosity that is necessary to explain the heat flow data in the oceanic areas (Fleitout & Yuen 1984; Dumoulin *et al.* 1999). It is also in good agreement with the interpretation of the post-glacial land emergence by Kaufmann & Wolf (1996) who found a sublithospheric viscosity in the range 10^{18}–10^{20} Pa s close to the continental margin and 10^{20}–10^{21} Pa s for locations inside the continent. The average lateral viscosity contrast between continental roots and the oceanic asthenosphere inferred from the gravity data in this study is somewhat higher than that estimated from the analysis of the global lithospheric rotation by Ricard *et al.* (1991) and Čadek & Ricard (1992) but it is much smaller than what can be deduced from the expected lateral temperature variations (Karato & Wu 1993).

The value of viscosity in the upper mantle ($\eta_{UM} \sim 3 \times 10^{20}$ Pa s) roughly agrees with the estimates based on an interpretation of the post-glacial rebound data (Peltier & Jiang 1996; Lambeck *et al.* 1998). In the lower mantle, however, the viscosity is found to be higher than the typical value estimated from post-glacial rebound. On the other hand, the value of η_{LM} inferred in the present study is in a good agreement with an independent estimate of the lower-mantle viscosity by Steinberger & O'Connell (1998) who studied the advection of plumes in the mantle flow. As recently proposed by Karato (1998) the discrepancies between various estimates of mantle viscosity may be associated with the existence of different types of rheologies that are relevant to various strain scales. It is also possible that the value of the lower-mantle viscosity inferred from the post-glacial rebound data may be underestimated as a result of neglecting the lateral viscosity variations in the uppermost mantle (Martinec *et al.* 2001).

As in the case without laterally variable viscosity (Čadek & Fleitout 1999), the velocity-to-density scaling factors $c_{UM} = 0$ and $c_{LM} = 0.2$ (eq. 16) provide the best fit to the gravitational data. The predicted value of c_{LM} is in a good agreement with a microphysical estimate of this parameter by Karato (1993), which suggests that the *S*-wave seismic velocity pattern is rather well correlated with the distribution of thermal anomalies in the lower mantle. In contrast, a zero correlation between the seismic and density anomalies ($c_{UM} = 0$) is obtained for the upper mantle. This result indicates that the large-scale seismic tomographic pattern of the upper mantle may be strongly affected by petrological and phase changes (Stevenson 1997; Weidner & Wang 2000). The fit to the data can be slightly improved if the density structure derived from the present-day location of slabs is imposed in the upper mantle (Section 2.4). The improvement is from 82 to 83 per cent for the geoid and from 47 to 50 per

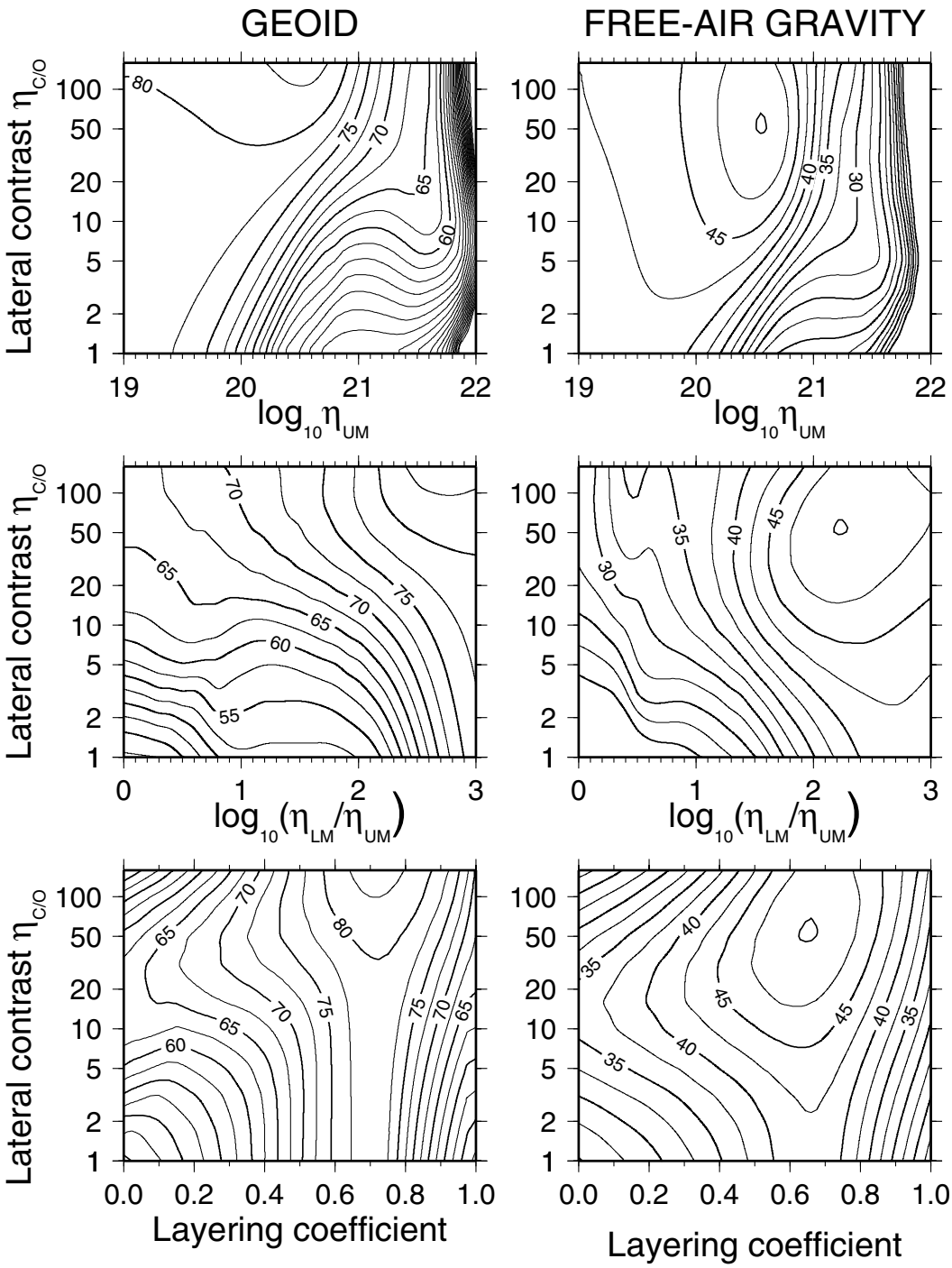

Figure 3. Maps of the maximum values of variance reduction P (eq. 18) plotted as functions of the lateral viscosity contrast $\eta_{C/O}$ and (top) the viscosity in the upper mantle η_{UM}, (middle) the viscosity increase η_{LM}/η_{UM} in the lower mantle, and (bottom) the layering coefficient λ (for exact definitions of the depicted quantities, see eqs 19–21 in Section 3.1). The left-hand panels show a percentage of the geoid predicted at degrees two to eight, while the results for the same spectral interval of the free-air gravity are shown on the right. The isoline interval is 2.5 per cent.

cent for the gravity anomalies. The best-fitting value of the scaling parameter χ (eq. 17) is found close to 1. It should be emphasized, however, that the role of the upper-mantle anomalies is minor and the major part of the gravitational signal is generated by the plate motion and the density anomalies located in the lower mantle. The slab density imposed in the upper mantle generates only one-tenth of the geoid signal induced by the loads in the lower mantle and one-fifth of the signal associated with the plate motion. The relative contribution of the slabs to the long-wavelength free-air gravity is somewhat larger but is still three times smaller than the contribution of the lower-mantle loads and twice as small as the signal induced by the plate motion.

Compared with the case without lateral viscosity variations, a relatively high viscosity in the upper mantle provides the best fit to the geoid and gravity (see the top panel of Fig. 3), while low upper-mantle viscosities without lateral viscosity variations still provide

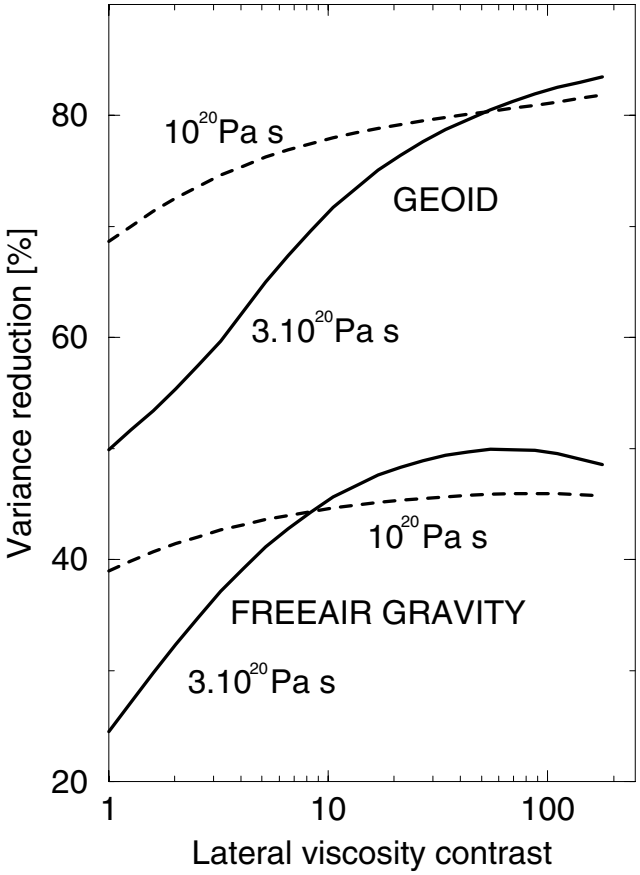

Figure 4. Maximum value of the variance reduction P as a function of the lateral viscosity contrast $\eta_{C/O}$ in the asthenosphere, depicted for two fixed values of viscosity in the upper mantle, $\eta_{UM} = 10^{20}$ Pa s (dashed lines) and 3×10^{20} Pa s (solid lines). The upper curves are for the geoid while prediction of the free-air gravity is illustrated in the bottom part of the figure.

an acceptable fit. The absolute value of the viscosity in the upper mantle mainly determines the amplitude of the contribution to the geoid owing to the surface plate velocities. Without the lateral viscosity variations, the geoid pattern induced by the plate velocities does not provide an acceptable component to the geoid. This component is thus damped in the inverse procedure by lowering the upper-mantle viscosity (Čadek & Fleitout 1999). With the lateral viscosity variations, the plate motion component to the geoid becomes more acceptable, mostly because the lows over ridges are less pronounced than the geoid highs over subduction zones. The upper-mantle viscosity is accordingly increased. This will lead in Section 4 to larger dynamic topography and tectonic stresses.

3.2 Effect of deep continental roots and young oceanic lithosphere

In Sections 3.1, we have considered a simple model of lateral viscosity variations corresponding to differences in average thickness between the oceanic and continental lithosphere. As a next step we will examine the effect of the deep lithospheric roots found in stable and cratonic continental regions. The distribution of the archaean cratons and stable continental platforms that are supposed to form the deep continental roots is based upon the map of Sclater *et al.* (1980) modified in Greenland and Eastern China in agreement with the more recent 3SMAC model by Nataf & Ricard (1996). In order

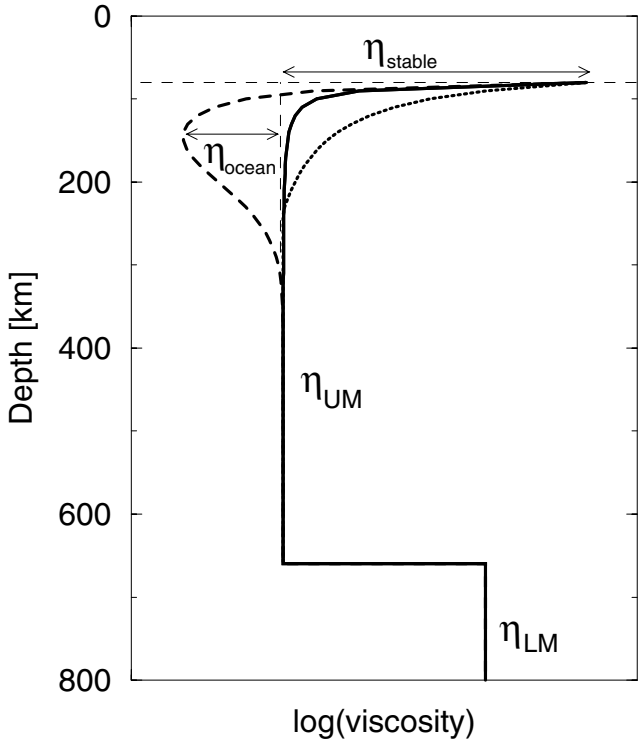

Figure 5. Viscosity structure considered in Section 3.2. Different viscosities are introduced below the oceanic lithosphere (η_{ocean}, dashed line), the young continental regions (solid line), and the cratonic and stable continental regions (dotted line). The lateral viscosity variations vanish at a depth of ~300 km. Below this depth the upper-mantle viscosity is represented by a single value η_{UM}. The viscosity in the lower mantle (η_{LM}) is independent of depth.

to avoid some technical difficulties our viscosity model is simplified in three respects. First, the boundary between the lithosphere and the surrounding mantle is not sharp but smoothed in both lateral and radial directions. Secondly, to avoid the difficulties associated with spectral evaluation of the boundary condition (13) in the case of a laterally variable viscosity, we construct all the viscosity profiles so that they start from the same value of viscosity in the uppermost point (Fig. 5). Thirdly, the maximum lateral viscosity contrast that can be managed by the spectral method described in Section 2 is $\sim 10^2$–10^3. Consequently, the continental roots cannot be modelled as effectively stiff if we want to keep a low viscosity ($\sim 10^{19}$ Pa s) for the oceanic asthenosphere. In spite of the above limitations we believe that such a simplified model is still useful because it can indicate whether the gravity data are compatible with the existence of deep lithospheric roots below the stable continental regions and how much these roots are important for predicting the gravitational response of the Earth.

Fig. 6 shows the maximum amount P_{max} of the predicted data,

$$P_{max}(\eta_{C/O}, \eta_{S/C}) \equiv \max_{\eta_{UM}, \eta_{LM}, \chi, c_{LM}, \lambda} P(\eta_{UM}, \eta_{LM}, \eta_{C/O}, \eta_{S/C}, \chi, c_{LM}, \lambda) \quad (22)$$

plotted as a function of the viscosity ratios $\eta_{S/C}$ ($\equiv \eta_{stable}/\eta_{UM}$) and $\eta_{C/O}$. The range of values investigated ($\eta_{S/C} \leq 30$, $\eta_{C/O} \leq 30$) corresponds to the intervals of stable convergence of the iterative method. The variance reduction increases with increasing value of $\eta_{S/C}$, reaching 55 per cent for free-air gravity and 85 per cent for the geoid. The viscosity structure that best fits the gravity is shown in Fig. 7. The models with high values of $\eta_{S/C}$ are generally

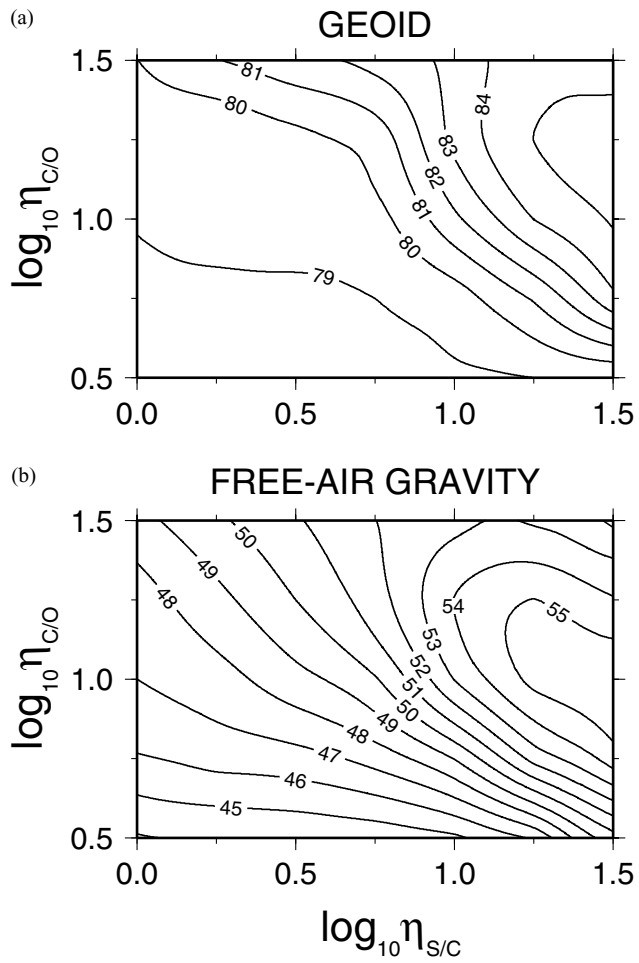

Figure 6. Maps of the maximum values of variance reduction P plotted as functions of the lateral viscosity contrasts $\eta_{C/O}$ and $\eta_{S/C}$ (for exact definition of the depicted quantity, see eq. 22 in Section 3.2). The percentage of the predicted geoid is shown in the top panel while the bottom panel shows the variance reduction obtained for the free-air gravity data. The isoline interval is 1 per cent.

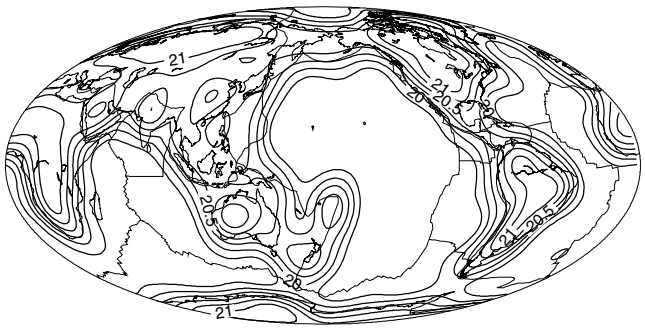

Figure 7. Lateral viscosity structure of the asthenosphere inferred from free-air gravity constraints. The geometry of the viscosity anomalies was *a priori* assumed on the basis of surface geology information (for more details, see Section 3.2). The viscosity pattern is shown at a depth of 120 km. The viscosity is plotted on a logarithmic scale. The isoline interval is 0.25.

characterized by smaller values of the viscosity ratio between the young subcontinental mantle and the oceanic asthenosphere ($\eta_{C/O} \sim 10$) in comparison with the models discussed in Section 3.1. The results shown in Fig. 6 suggest that the long-wavelength

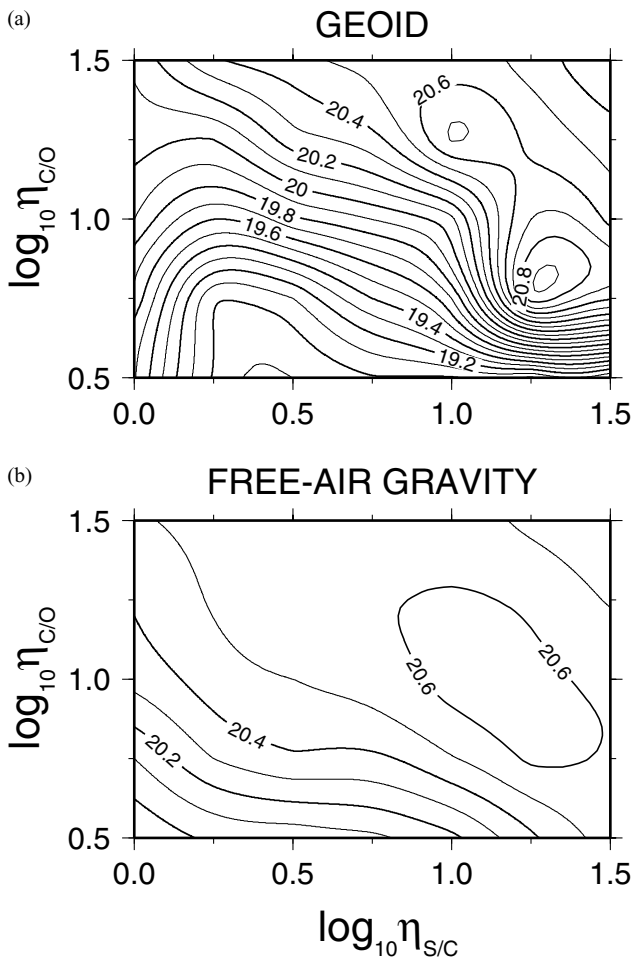

Figure 8. Logarithmic value of the viscosity in the upper mantle (η_{UM}) that yields the best fit to (top) geoid and (bottom) free-air gravity as a function of the lateral viscosity contrasts $\eta_{C/O}$ and $\eta_{S/C}$ (for definitions of the parameters, see Section 3.2). The isoline interval is 0.1. The corresponding variance reduction can be deduced from Fig. 6.

data are compatible with the concept of highly viscous lithospheric roots expected below the stable continental regions. However, this conclusion cannot be verified for effectively stiff continental roots because of the unstable behaviour of the spectral method in the case of large lateral gradients in viscosity.

The viscosity η_{UM} that yields the maximum value P_{max} of the variance reduction P, eq. (22), is depicted in Fig. 8 as a function of the viscosity contrasts $\eta_{C/O}$ and $\eta_{S/C}$. The figure is organized in the same way as Fig. 6 where the corresponding percentage of the predicted data can be deduced. A comparison of Figs 6 and 8 shows that there is good agreement between the values of η_{UM} that predict the best geoid (for $P \geq 85$ per cent, $2.5 \times 10^{20} \leq \eta_{UM} \leq 5 \times 10^{20}$ Pa s) and those inferred from the free-air gravity data ($3.5 \times 10^{20} \geq \eta_{UM} \geq 4.5 \times 10^{20}$ Pa s if $P \geq 55$ per cent). These values are compatible with the estimates of upper-mantle viscosity from the post-glacial rebound data (Peltier & Jiang 1996; Lambeck *et al.* 1998). The values of viscosity deduced for the lower mantle (Fig. 9) are less unique. The lower-mantle viscosity for the models that best fit the geoid is two to three times higher than for the models inferred from the free-air gravity data. Since the geoid is more sensitive to the viscosity structure in the deep lower mantle than the free-air gravity, this discrepancy may indicate that the viscosity in the lower mantle

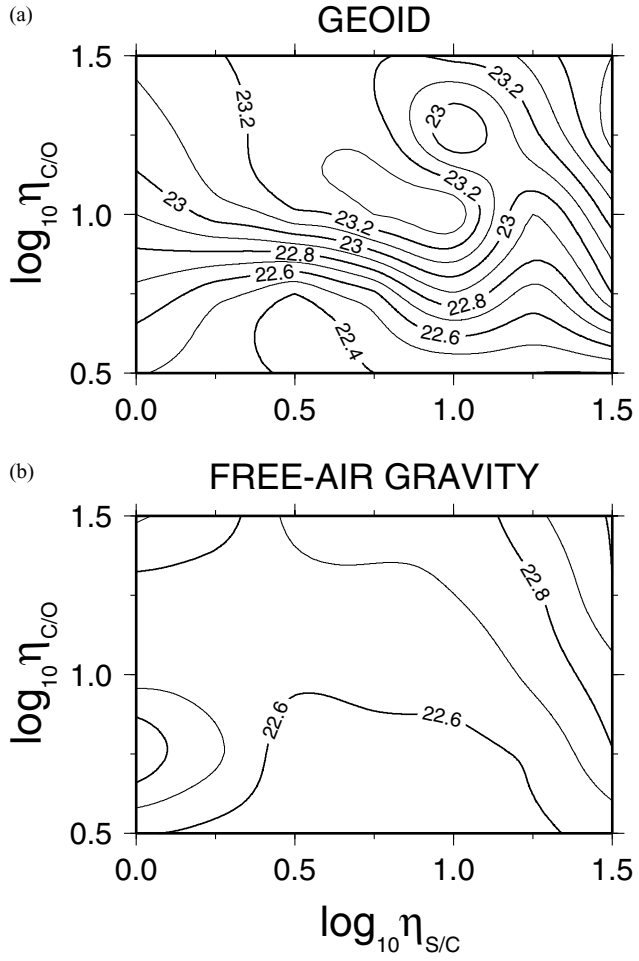

Figure 9. Logarithmic value of the viscosity in the lower mantle (η_{LM}) that yields the best fit to (a) geoid and (b) free-air gravity as a function of the lateral viscosity contrasts $\eta_{C/O}$ and $\eta_{S/C}$ (for definitions of the parameters, see Section 3.2). The isoline interval is 0.1. The corresponding values of variance reduction and viscosity η_{UM} can be deduced from Figs 6 and 8, respectively.

is not a constant, as is assumed in the present study, but increases with depth (Karato 1996). If this is the case, the value of $\eta_{LM} \sim 2 \times 10^{23}$ Pa s inferred from the geoid represents the viscosity in the bottom part of the lower mantle while the value of $\sim 6 \times 10^{22}$ Pa s derived from the free-air gravity may be typical for the top part of the lower mantle. The latter value is indeed rather close to estimates of the lower-mantle viscosity deduced from the rebound analyses of small- and medium-scale glaciers that mainly sample the upper and shallow lower mantles (Lambeck *et al.* 1996, 1998). The reader should also be aware that our estimate of η_{LM} may be affected by a simplified scaling of the tomographic model in the lower mantle (c_{LM} in eq. 16 is assumed to be constant throughout the lower mantle), by neglecting the effects of lateral viscosity variations below a depth of 400 km, and by simplifying the boundary condition at the core–mantle boundary (CMB) where free slip, eq. (8), may not be adequate for the complex physical situation expected in the D″.

Since the thickness of the oceanic lithosphere varies with the age of the lithosphere, one can expect the mantle close to the mid-oceanic ridges to be weaker than below old oceanic provinces. We have tested this hypothesis assuming that the logarithmic value of viscosity in the asthenosphere is proportional to the square root of the age of the oceanic lithosphere. The results of these tests, however, have shown only minor effects on the geoid and the free-air gravity prediction. The analysis is complicated by a trade-off between the values of viscosity below the young and old oceanic lithospheres: the variance reduction P does not change if decreasing viscosity below the ridges is accompanied by a modest increase in viscosity below the old oceanic provinces. Thus, the fit to the geoid obtained for a viscosity of 1×10^{18} Pa s below the ridges and 2×10^{19} Pa s below the old oceanic lithosphere is the same as that obtained for the model with a constant viscosity of 1×10^{19} Pa s imposed throughout the oceanic asthenosphere. The effect of lateral changes in viscosity beneath the oceanic regions will be discussed further in Section 3.4.

The prediction of the gravitational response of the Earth may be affected by the lateral variations of viscosity in the deep mantle (Zhong & Davies 1999). The main rheological anomalies in the deep mantle are presumably associated with the distribution of subducted lithosphere. Using a long-wavelength approximation (cut-off degree 24), we have investigated the effect of highly viscous slabs in the upper mantle imposed together with the viscosity structure II discussed in Section 3.1. In spite of an extensive exploration of the model space we have found no model that would significantly improve the prediction of the gravitational signal. It is obvious that this kind of viscosity structure requires an extremely high spatial resolution that cannot be presently reached by the spectral method (for recent results from the finite-element modelling see Zhong & Davies 1999).

3.3 Effect of a viscosity increase in the transition zone

Until now we have considered the models in which the radial viscosity structure has been parametrized by only two values of viscosity, η_{UM} and η_{LM}, characterizing the average viscosity in the upper and lower mantle, respectively. We have tested whether the gravitational data can be used to constrain the value of viscosity in the transition zone. This value may differ from the average viscosity in the shallow upper mantle (Karato *et al.* 1995). We have parametrized the radial viscosity structure of the mantle by three variables, corresponding to viscosities at depth intervals of 80–410, 410–660 and 660–2890 km, while two parameters, $\eta_{S/C}$ and $\eta_{C/O}$ introduced in Section 3.2, have been used to characterize the lateral viscosity variations in the top 300 km of the mantle. The considered velocity-to-density scaling parameters are the same as in Section 3.1.

In spite of a higher number of free parameters, we have reached no substantial improvement in predicting the geoid and free-air gravity data in comparison with the models investigated in Section 3.2. The best fit to the data has been obtained for the viscosity profiles that show no or only a weak (by a factor of 2) increase in viscosity at 410 km. However, more than 83 per cent of the geoid and 50 per cent of the gravity can be predicted even if the viscosity at 410 km increases by one to two orders of magnitude. In contrast, a pronounced low-viscosity transition zone significantly deteriorates the fit to the gravitational data. We have also tested the influence of a narrow (100 km thick) low-viscosity zone imposed either above or below the 660 km interface, but we have found no improvement of the fit (*cf.* Forte *et al.* 1993; Kido & Čadek 1997).

3.4 Asthenospheric viscosity structure inferred from geoid and gravity data

The models of lateral viscosity variation investigated in Sections 3.1–3.3 have been defined on the basis of surface geology. The geometry of the viscosity anomalies has been given *a priori*

and the observed gravitational signal has been employed only to optimize the amplitudes. The question arises of whether the viscosity structures considered above really yield the optimum prediction of the gravitational information. To clarify this issue we will search for the distribution of viscosity in the asthenosphere that provides the best fit to the geoid and free-air gravity data. In contrast to Sections 3.1–3.3 we will consider no *a priori* model of viscosity anomalies but we will directly determine the coefficients of a viscosity field. To keep the number of free parameters reasonably low we only consider a spherical harmonic series up to degree four on a logarithmic scale:

$$\log_{10}\eta(\vartheta,\phi) = \sum_{\ell=0}^{4}\sum_{m=-\ell}^{\ell}\eta_{\ell m}Y_{\ell m}(\vartheta,\phi), \tag{23}$$

where $Y_{\ell m}$ are the fully normalized complex spherical harmonics and $\eta_{\ell m}$ are the spherical harmonic coefficients that are to be determined. As in Section 3.1, we assume that the maximum lateral contrast in viscosity occurs at a depth of ∼150 km. The lateral viscosity variations are damped towards the surface and the deeper mantle in the same way as $\eta_{\rm ocean}$ in Fig. 2. The mantle below the asthenosphere is characterized by parameters $\eta_{\rm UM}$, $\eta_{\rm LM}$ and λ (for definitions, see Sections 2.4 and 3.1). In the upper mantle the density distribution derived from the present-day location of slabs is imposed while the tomography-based density anomalies, scaled by an unknown model parameter $c_{\rm LM}$, eq. (16), are considered for the lower mantle. To find the values of the model parameters that best predict the observed gravitational signal we use the method of simulated annealing (Press *et al.* 1992). For the reasons of fast convergence of the iterative method (Section 2.1) only the models with lateral viscosity contrasts smaller than three orders of magnitude are taken into account.

The resulting model of lateral viscosity variations in the asthenosphere is shown in Fig. 10. The optimum values of the parameters characterizing the spherically symmetric part of the model are $\eta_{\rm UM} = 3 \times 10^{20}$ Pa s, $\eta_{\rm LM} = 3 \times 10^{22}$ Pa s, $c_{\rm LM} = 0.14$ and $\lambda = 0.60$. The robustness of the resulting viscosity model has been tested by solving the inverse problem several times for randomly chosen starting models. The solutions obtained for individual runs show basically the same pattern of lateral viscosity variations in the asthenosphere as in Fig. 10, but they may differ somewhat in the other parameters. The best-fitting model predicts 67 per cent of the free-air gravity data and more than 90 per cent of the geoid. These values are significantly larger than those obtained for the models with an *a priori* imposed pattern of viscosity anomalies (Sections 3.1–3.3). The fit to the data is illustrated in Fig. 11. The present model predicts reasonably well the gravitational signal for all the degrees between two and eight (Fig. 12). Thus, the same set of parameters provides a very good fit to both the geoid and gravity. A comparison of the two correlation curves in Fig. 12 indicates that the lateral viscosity variations mainly affect the higher degrees, in particular degree six.

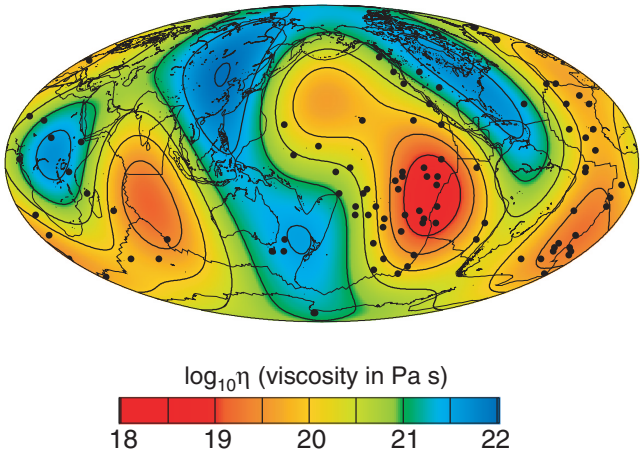

Figure 10. Lateral viscosity variations in the asthenosphere inferred from the geoid and free-air gravity constraints without using any *a priori* viscosity model. The viscosity is plotted in logarithmic scale with an isoline interval of 0.5. The black dots mark present-day positions of the hotspots (Nataf & Ricard 1996).

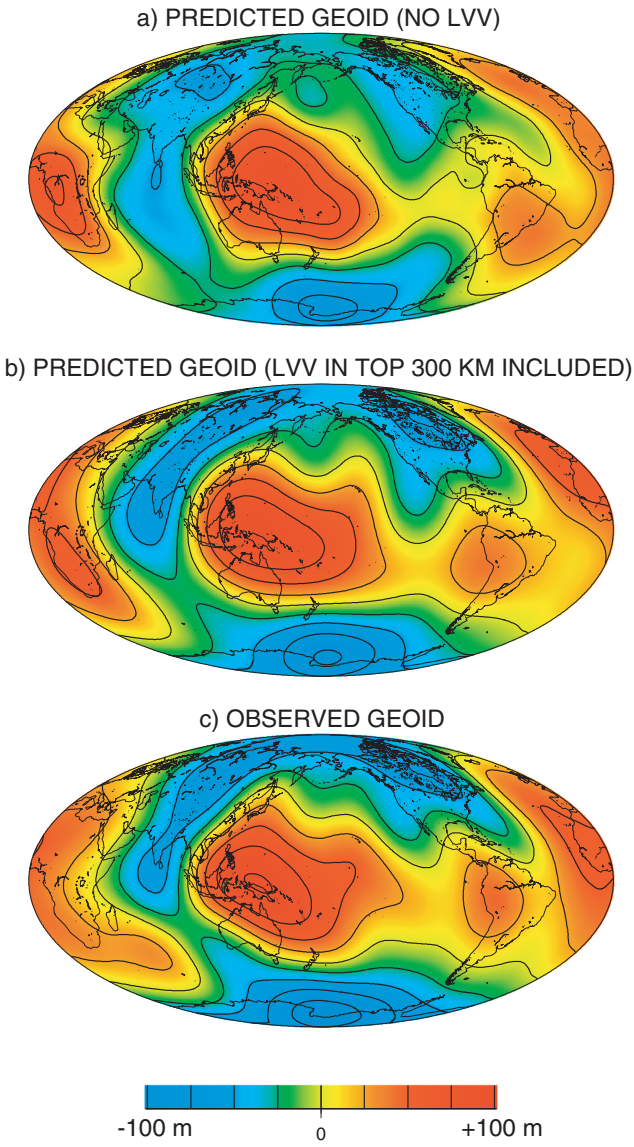

Figure 11. (a) Geoid predicted by Čadek & Fleitout (1999) for a flow model with radially dependent viscosity. (b) Geoid predicted in the present study for a viscosity model including laterally variable viscosity in the top 300 km and radially variable viscosity in a deeper mantle. (c) Observed non-hydrostatic geoid ($\ell = 2$–8) corrected for the lithospheric effects (Doin *et al.* 1996). The model geoids in panels (a) and (b) predict, respectively, 76 and 92 per cent of the observed signal.

The pattern of viscosity anomalies in Fig. 10 shows a clear similarity to the viscosity models based on surface geology (Figs 1b and 7). The regions of higher-than-average viscosity correlate well

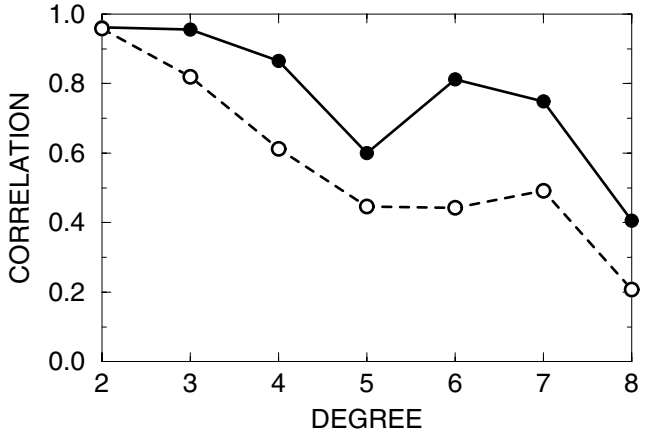

Figure 12. Degree-by-degree correlation between the observed geoid and the geoid predicted (dashed line) for the flow model without lateral viscosity variations, and (full line) for the viscosity structure discussed in Section 3.4.

with the distribution of the continents. A relatively high viscosity is also found beneath most subduction zones, including the South-West Pacific. The resolution of the viscosity model is not sufficient for a more detailed structure of the continental regions to be revealed. The viscosity minima are located below the East-Pacific Rise and the Indian Ridge. In the Atlantic Ocean, the local minimum of viscosity is correlated with the distribution of the hotspots rather than with the Mid-Atlantic Ridge. The result of the inversion confirms the assumption that the lateral viscosity variations in the top 300 km of the mantle are mainly controlled by the present-day positions of the continents. The viscosity difference between the continental and oceanic regions predicted in our models is probably a reflection of the different thickness of the lithosphere beneath continents and oceans. As was already discussed in Section 3.1, a satisfactory prediction of the gravity signal can be obtained only if a higher-than-average viscosity is imposed beneath the main subduction zones. In contrast to Section 3.2, our inversion confirms the existence of anomalously low-viscosity regions beneath the ridges and the hotspot superswells.

The major part of the predicted geoid is generated by the plate motion and the density anomalies located in the lower mantle ($|G^{\mathrm{pred}}_{\mathrm{plates}}|_{\mathrm{L}_2}/|G^{\mathrm{obs}}|_{\mathrm{L}_2} = 0.73$ and $|G^{\mathrm{pred}}_{\mathrm{LM}}|_{\mathrm{L}_2}/|G^{\mathrm{obs}}|_{\mathrm{L}_2} = 0.72$), while the signal caused by the slabs imposed in the upper mantle is less important ($|G^{\mathrm{pred}}_{\mathrm{slabs}}|_{\mathrm{L}_2}/|G^{\mathrm{obs}}|_{\mathrm{L}_2} = 0.05$). The relative contribution of the slabs to the long-wavelength gravity signal is somewhat larger (0.11) but still significantly smaller than the signal induced by the plates (0.61) and the lower-mantle loads (0.57).

4 DYNAMIC CHARACTERISTICS OF THE MODEL

4.1 Topography of the 660 km discontinuity

The layering coefficient λ (Section 2.3) can be interpreted in terms of mass anomalies that resist the mass flux across the 660 km discontinuity (Čadek & Fleitout 1999). In reality, these masses can be spread over a large depth interval, especially if they represent petrological variations in the mantle. The usual way to visualize these anomalies is to recompute them in terms of deflections of the density interface separating the upper and lower mantles (Thoraval *et al.* 1995; Le Stunff & Ricard 1997; Čadek & Fleitout 1999). The topography of the 660 km discontinuity predicted for the flow model discussed in Section 3.4 is given in Fig. 13. The topographies corresponding to the models derived on the basis of *a priori* geological information (Sections 3.1–3.3) differ from that in Fig. 13 only in details. The topography predicted by our flow models shows the same amplitudes ($\pm$15 km) as the topography obtained from seismic inversions (Flanagan & Shearer 1998). A good correlation between our prediction and seismic observation is found for the eastern hemisphere. In contrast, a significant discrepancy between the models is found below the Pacific and the Americas where our dynamic model predicts pronounced topographic anomalies associated with the East-Pacific subduction and with a large-scale upwelling in the lower mantle below the central Pacific. Concerning the flow situation at the 660 km discontinuity, our flow models with lateral viscosity variations show basically the same flow patterns at this depth as the models obtained by Čadek & Fleitout (1999) for radially stratified viscosity structures. For more details, the reader is referred to Section 3.6 in Čadek & Fleitout (1999) where the flow field at the 660 km discontinuity is plotted for different viscosity structures.

4.2 Dynamic topography

The dynamic surface topography is usually defined as a topographic signal maintained by the flow in a sublithospheric mantle. The dynamic topography obviously differs from the observed topography, which is mostly related to isostatic compensation of crustal thickness variations and to thermal cooling of the oceanic lithosphere (for a detailed discussion of the concept of dynamic topography see Le Stunff & Ricard 1995). The amplitudes of the dynamic topography are significantly smaller than the observed topographic amplitudes. The analysis of the geological data suggests that the amplitudes of the large-scale dynamic topography over the oceans should not exceed some 500 m (Colin & Fleitout 1990; Le Stunff & Ricard 1995).

The shape of the dynamic topography is not known. The simplified estimates of the dynamic topography based on whole-mantle flow models with a free-slip upper boundary usually show large topographic depressions in the neighbourhood of subduction zones (Hager & Clayton 1989) while elevations are obtained close to ridges and the regions of hotspots activity (Lithgow-Bertelloni & Silver 1998). This paradigm may be misleading, however, since the shape of the dynamic topography is probably strongly influenced by the existence of stiff lithospheric plates and by a complex flow situation at 660 km. As demonstrated by Čadek *et al.* (1998) for a model with a free-slip upper boundary, the large-scale dynamic topography may be weakly positive in the neighbourhood of subduction zones provided that the mantle convection is layered. The lithospheric plates induce a similar effect. If the plates are mainly driven by mass heterogeneities near the boundaries (slab pull), then the lithosphere drags the underlying mantle, giving rise to a large-scale flow. This flow may generate a positive large-scale topography above the convergent plate boundaries and a negative topography close to the spreading centres (Ricard *et al.* 1988; Karpychev & Fleitout 1996). In both cases discussed above the positive large-scale topography above the subduction zone is overprinted by a negative small-scale topography at a short distance from the trench.

The traditional intuitive view linking the subduction zones to negative dynamic topography and the ridges to positive dynamic topography is also questioned by the oceanic bathymetric data corrected for thermal effects (Colin & Fleitout 1990; Panasyuk & Hager 2000). These data suggest a dynamic topography increasing from slightly negative values in the neighbourhood of the East-Pacific

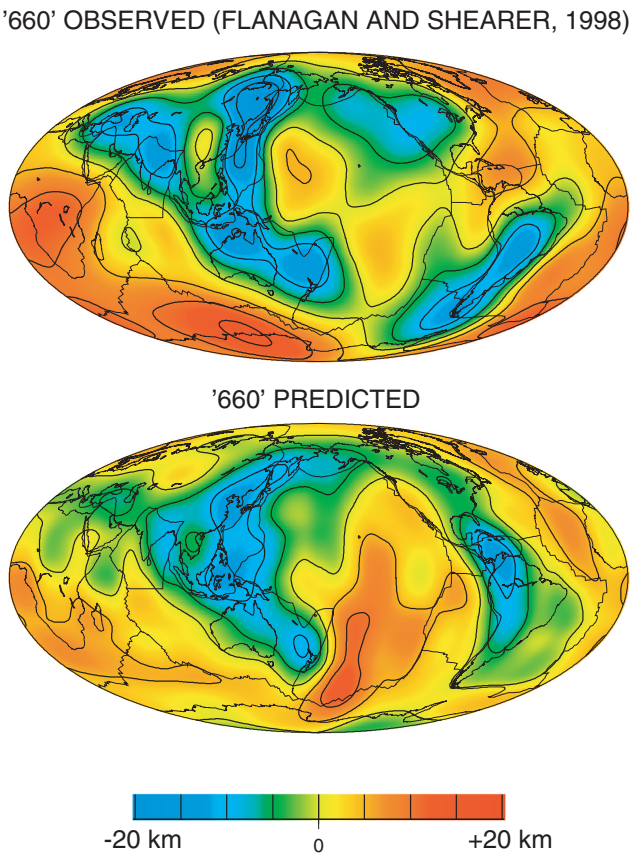

Figure 13. Comparison between (a) observed (Flanagan & Shearer 1998) and (b) predicted topography of the 660 km discontinuity. A density contrast of 390 kg m^{-3} between the upper- and lower-mantle materials has been considered (Dziewonski & Anderson 1981). Both maps are plotted for the degrees $\ell = 1$–12. The isoline interval is 5 km.

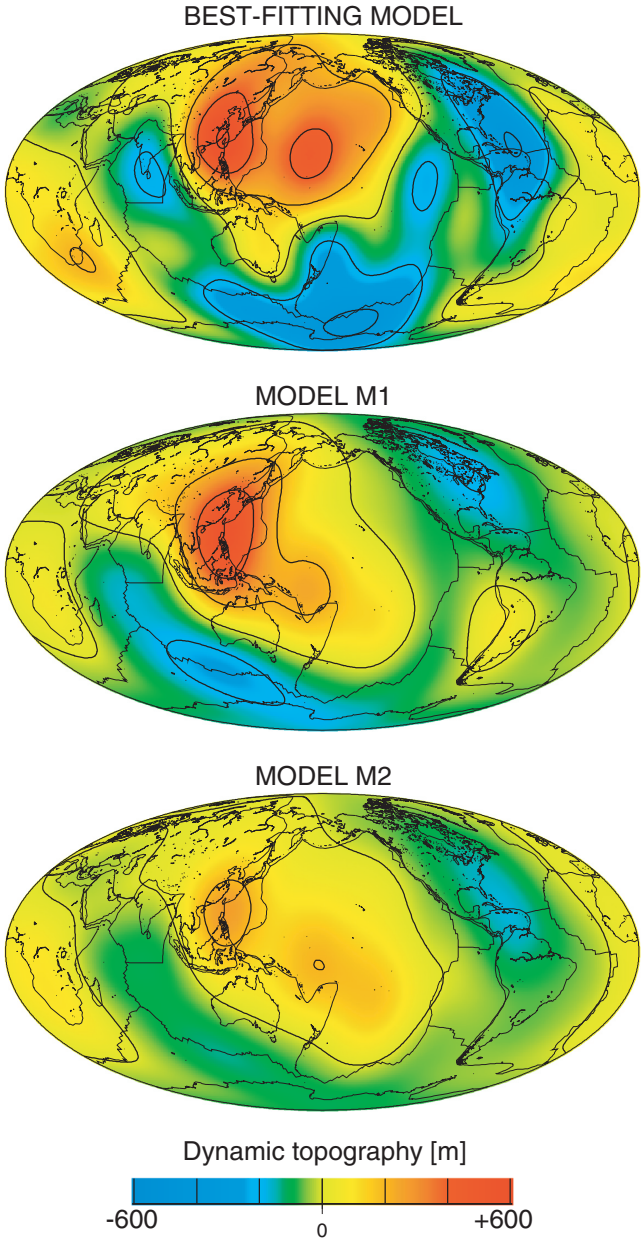

Figure 14. Surface dynamic topography corresponding to different flow models providing an acceptable fit to the gravitational data. The top panel shows the model obtained without *a priori* information on the lateral viscosity structure (for the parameters, see Section 3.4). The other two panels (models M1 and M2) illustrate the dynamic topographies computed for lateral viscosity structures based on surface geology (Sections 3.1–3.3). Basic characteristics of models M1 and M2 can be found in Table 1. Only the low-degree ($\ell = 1$–8) part of the topographic signal is shown. The isoline interval is 200 m.

Rise to positive values in the West Pacific. Our prediction of the long-wavelength dynamic topography based on the inversion of the geoid confirms this trend. Three examples of the dynamic surface topography obtained for the flow models that predict a significant amount of the geoid and free-air gravity data are depicted in Fig. 14. The top panel shows the topography corresponding to the flow model derived without *a priori* information on the distribution of lateral viscosity variations (Section 3.4). The other two panels (models M1 and M2) correspond to models based on actual ocean–continent distributions (Section 3.1–3.3). Their characteristics are given in Table 1. All three models show basically the same pattern of long-wavelength dynamic topography: the topographic maximum is found in South–East Asia while the main depressions are located close to mid-ocean ridges and in North America. A local maximum is usually found in South Africa. The topographic amplitudes are significantly smaller than those usually predicted for the case of the whole mantle. However, their magnitude is not well constrained: it amounts to 600 m in the case of the best-fitting model but only to 300 m in the case of model M2. The amplitude of the dynamic topography mainly depends on the viscosity below the lithosphere, which determines the intensity of basal drag, and on the density assumed for the slabs in the upper mantle. It is important to realize that the slab densities, especially those located in a shallow mantle, do not influence much the prediction of the long-wavelength gravitational data but they may significantly contribute to the dynamic topography (to understand this effect, see the geoid and topographic kernels in Ricard *et al.* 1984 and Hager & Clayton 1989). The models with a relatively high upper-mantle viscosity imply a large topographic component linked to the plate motion (top panel in Fig. 14). In contrast, the total dynamic topography in model M2 is reduced owing to a small upper-mantle viscosity and larger upper-mantle loads.

We emphasize that the presented models show only the low-degree part of the topographic signal ($\ell = 1$–8). The topography pattern that we propose here (positive topography in the neighbourhood of subduction zones) can certainly be questioned at

Table 1. Basic characteristics of models M1 and M2 (Fig. 14).

Model	λ	χ	c_{LM}	$\eta_{C/O}$	$\eta_{S/C}$	η_{UM} (Pa s)	η_{LM} (Pa s)	P_{geoid} (per cent)	P_{grav} (per cent)
M1	0.67	0.8	0.19	10	30	2.4×10^{20}	7.7×10^{22}	82.6	51.3
M2	0.64	1.2	0.20	10	30	1.2×10^{20}	4.8×10^{22}	80.0	50.0

short wavelengths: as mentioned earlier we are not able to treat short-wavelength viscosity variations. The stresses transmitted through the stiff slabs may in reality induce topographic depressions that are more focused than those presented by Hager & Clayton (1989). The exact signal linked to the subduction zones is difficult to model as it requires good knowledge of the detailed rheology in the plate boundary area and of the processes at 660 km depth. This signal is of minor importance for the computation of the global geoid as mentioned earlier. However, it may affect the topography at a short distance from the subduction zones and a relatively narrow topographic low may be superimposed on the broad topographic high proposed in Fig. 14 (Čadek *et al.* 1998).

5 CONCLUSIONS

This paper has tested the effect of a variable viscosity in the top upper mantle on the prediction of the geoid from the observed plate motions and internal loading. As discussed in the previous paper (Čadek & Fleitout 1999), one must bear in mind that the model presented here is far from perfect: the 'partial layering' is a simple parametrization of not yet well understood phenomena hampering the flow of matter across the transition zone. The density anomalies may not be simply proportional to seismic velocities either, especially in the case of petrological heterogeneities. Some outputs of our study, namely the predicted pattern of the dynamic surface topography, may be affected by the limited resolution of the spectral method that can hardly take into account sharp plate boundaries and small-scale heterogeneities associated with subducting slabs. In spite of these limitations, the models presented here have clearly shown that the lateral viscosity variations are an important ingredient to introduce in the geoid computation.

Unlike the geoid component linked to deep loads, the geoid component linked to plate velocities is considerably modulated by LVV. In a previous paper (Čadek & Fleitout 1999), the geoid induced by the plate motion did not provide an acceptable contribution to the geoid. Consequently, the minimization method used to find the viscosity structure producing the best fit to the geoid kept only the geoid component linked to the internal loading and suppressed the component linked to the plate motion. The best prediction of the geoid was obtained for rather low values of viscosity in the upper mantle. When lateral viscosity variations are taken into account, the plate velocity component contributes to improve the fit to the geoid. Consequently, larger viscosities in the upper mantle are needed to make this term relatively important. This implies larger stresses and topography, especially at degree one. There is, however, a trade-off between the value of viscosity in the top and the bottom upper mantle. A low-viscosity channel below the lithosphere provides a good fit to the geoid and lowers the stresses and topography. Since the global pattern of the stress and topographic signal does not change considerably while the amplitude changes, we believe that a comparison of the topography found here with the real residual topography in the oceans may provide important additional constraints on the viscosity models. Further improvements of the model may be obtained after including larger viscosity contrasts, a finer resolution and a more detailed description of subduction zones.

ACKNOWLEDGMENTS

We are grateful to Harro Schmeling and Bernard Steinberger for comments and constructive criticism. This work has been supported by Czech national grant nos 205/99/0256 and 205/02/1306.

REFERENCES

Čadek, O. & Ricard, Y., 1992. Toroidal/poloidal energy partitioning and global lithospheric rotation, *Earth planet. Sci. Lett.*, **109,** 621–632.

Čadek, O. & Fleitout, L., 1999. A geoid model with imposed plate velocities and partial layering, *J. geophys. Res.*, **104,** 29 055–29 075.

Čadek, O., Martinec, Z. & Matyska, C., 1992. Spectral variational approach to the non-Newtonian Stokes problem in a spherical shell, *Comput. Phys. Commun.*, **71,** 56–70.

Čadek, O., Ricard, Y., Martinec, Z. & Matyska, C., 1993. Comparison between Newtonian and non-Newtonian flow driven by internal loads, *Geophys. J. Int.* **112,** 103–114.

Čadek, O., Yuen, D.A. & Čížková, 1998. Mantle viscosity inferred from geoid and seismic tomography by genetic algorithms: results for layered mantle flow, *Phys. Chem. Earth*, **23,** 865–872.

Christensen, U.R., 1998. Dynamic phase boundary topography by latent heat effects, *Earth planet. Sci. Lett.*, **154,** 295–306.

Colin, P., 1993. Geoid global, tomographie associée et structure de la convection dans le manteau terrestre: Modelisation and observation, *PhD thesis,* Ecole Normale Supérieure, Paris.

Colin, P. & Fleitout, L., 1990. Topography of the oceanic floor: thermal evolution of the lithosphere and interaction of deep mantle heterogeneities with the lithosphere, *Geophys. Res. Lett.*, **17,** 1961–1964.

Corrieu, V., Ricard, Y. & Froidevaux, C., 1994. Converting mantle tomography into mass anomalies to predict the Earth's radial viscosity, *Phys. Earth planet. Inter.*, **84,** 3–13.

D'Agostino, G., Spada, G. & Sabadini, R., 1997. Postglacial rebound and lateral viscosity variations: a semi-analytical approach based on a spherical model with Maxwell rheology, *Geophys. J. Int.* **129,** F9–F13.

Doin, M.-P. & Fleitout, L., 1997. Thermal evolution of the oceanic lithosphere: an alternative view, *Earth planet. Sci. Lett.*, **142,** 121–136.

Doin, M.-P., Fleitout, L. & McKenzie, D., 1996. Geoid anomalies and the structure of continental and oceanic lithospheres, *J. geophys. Res.*, **101,** 16 119–16 135.

Dumoulin, C., Doin, M.-P. & Fleitout, 1999. Heat transport in stagnant lid convection with temperature- and pressure-dependent Newtonian or non-Newtonian rheology, *J. geophys. Res.*, **104,** 12 759–12 777.

Dziewonski, A.M. & Anderson, D.L., 1981. Preliminary Reference Earth Model (PREM), *Phys. Earth planet. Inter.*, **25,** 297–356.

Flanagan, M.P. & Shearer, P.M., 1998. Global mapping of topography on transition zone velocity discontinuities by stacking SS precursors, *J. geophys. Res.*, **103,** 2673–2692.

Fleitout, L. & Yuen, D.A., 1984. Secondary convection and growth of oceanic lithosphere, *Phys. Earth planet. Inter.*, **36,** 181–212.

Forsyth, D. & Uyeda, S., 1975. On the relative importance of the driving forces of plate motion, *Geophys. J. R. astr. Soc.*, **43,** 163–200.

Forte, A.M. & Peltier, W.R., 1994. The kinematics and dynamics of poloidal–toroidal coupling in mantle flow: the importance of surface plates and lateral viscosity variations, *Adv. Geophys.*, **36,** 1–119.

Forte, A.M., Dziewonski, A.M. & Woodward, R.L., 1993. Aspherical structure of the mantle, tectonic plate motions, nonhydrostatic geoid, and topography of the core–mantle boundary, in *Dynamics of Earth's Deep Interior and Earth Rotation*, Vol. 72, pp. 135–166, eds Le Mouël, J.L., Smylie, D.E. & Herring, T., *Geophys. Monograph Ser.*, AGU, Washington, DC.

Forte, A.M., Woodward, R.L. & Dziewonski, A.M., 1994. Joint inversions of seismic and geodynamical data for models of three-dimensional mantle heterogeneity, *J. geophys. Res.*, **99,** 21 857–21 877.

Gasperini, P., Sabadini, R. & Yuen, D.A., 1991. Deep continental roots: the effect of lateral variations of viscosity on post-glacial rebound, in *Glacial Isostasy, Sea-Level and Mantle Rheology*, pp. 21–32, eds Sabadini R. *et al.*, Kluwer, Dordrecht.

Hager, B.H. & Clayton, R.W., 1989. Constraints on the structure of mantle convection using seismic observations, flow models, and the geoid, in *Mantle Convection: Plate Tectonics and Global Dynamics*, pp. 657–763, ed., Peltier, W.R., Gordon and Breach, Newark, N.J.

Hager, B.H. & O'Connell, R.J., 1979. Kinematic models of large-scale flow in the Earth's mantle, *J. geophys. Res.*, **84,** 1031–1048.

Hager, B.H. & O'Connell, R.J., 1981. A simple global model of plate dynamics and mantle convection, *J. geophys. Res.*, **86,** 4843–4867.

Karato, S., 1993. Importance of anelasticity in the interpretation of seismic tomography, *Geophys. Res. Lett.*, **20,** 1623–1626.

Karato, S., 1996. Phase transformations and rheological properties of mantle materials, in *Earth's Deep Interior*, chapter 8, eds Crossley, D. & Soward, A.M., Gordon and Breach, New York.

Karato, S., 1998. Micro-physics of post glacial rebound, in *Dynamics of the Ice Age Earth: a Modern Perspective*, pp. 351–364, ed., Wu, P., Trans Tech, Zurich, Switzerland.

Karato, S. & Wu, P., 1993. Rheology of the upper mantle: a synthesis, *Science*, **260,** 771–778.

Karato, S., Wang, Z., Liu, B. & Fujino, K., 1995. Plastic deformations of garnets: systematics and implications for the rheology of the mantle transition zone, *Earth planet. Sci. Lett.*, **131,** 13–31.

Karpychev, M. & Fleitout, L., 1996. Simple considerations on forces driving plate motion and on the plate-tectonic contribution to the long-wavelength geoid, *Geophys. J. Int.* **127,** 268–282.

Karpychev, M. & Fleitout, L., 2000. Long-wavelength geoid: the effect of continental roots and lithosphere thickness variations, *Geophys. J. Int.* **143,** 945–963.

Kaufmann, G. & Wolf, D., 1996. Deglacial land emergence and lateral upper-mantle heterogeneity in the Svalbard Archipelago, II, Extended results for high-resolution load models, *Geophys. J. Int.* **127,** 125–140.

Kaufmann, G., Wu, P. & Li, G., 2000. Glacial isostatic adjustment in Fennoscandia for laterally heterogeneous earth, *Geophys. J. Int.* **143,** 262–273.

Kido, M. & Čadek, O., 1997. Inferences of viscosity from oceanic geoid: indication of a low viscosity zone below the 660 km discontinuity, *Earth planet. Sci. Lett.*, **151,** 125–138.

King, S.D., 1995a. Models of mantle viscosity, in *Mineral Physics & Crystallography, a Handbook of Physical Constants*, pp. 227–236, ed., Ahrens, T.J., *AGU Reference Shelf 2,* AGU, Washington, DC.

King, S.D., 1995b. Radial models of mantle viscosity: results from a genetic algorithm, *Geophys. J. Int.* **122,** 725–734.

King, S.D. & Hager, B.H., 1994. Subducted slabs and the geoid: 1) numerical calculations with temperature-dependent viscosity, *J. geophys. Res.*, **99**, 19 843–19 852.

Lambeck, K., Johnston, P., Smither, C. & Nakada, M., 1996. Glacial rebound of the British Isles, III, Constraints on mantle viscosity, *Geophys. J. Int.* **125,** 340–354.

Lambeck, K., Smither, C. & Johnston, P., 1998. Sea-level change, glacial rebound and mantle viscosity for northern Europe, *Geophys. J. Int.* **134,** 102–144.

Le Stunff, Y. & Ricard, Y., 1995. Topography and geoid due to lithospheric mass anomalies, *Geophys. J. Int.* **122,** 982–990.

Le Stunff, Y. & Ricard, Y., 1997. Partial advection of equidensity surfaces: a solution for the dynamic topography problem?, *J. geophys. Res.*, **102**, 24 655–24 667.

Lithgow-Bertelloni, C. & Richards, M.A., 1998. The dynamics of Cenozoic and Mesozoic plate motions, *Rev. Geophys.*, **36,** 27–78.

Lithgow-Bertelloni, C. & Silver, P.G., 1998. Dynamic topography, plate driving forces and the African superswell, *Nature*, **395,** 269–272.

Manga, M. & O'Connell, R.J., 1995. The tectosphere and postglacial rebound., *Geophys. Res. Lett.*, **22,** 1949–1952.

Martinec, Z., 1989. Program to calculate the spectral harmonic expansion coefficients of the two scalar fields product, *Comput. Phys. Commun.*, **54,** 177–182.

Martinec, Z., 1999. Spectral, initial value approach for viscoelastic relaxation of a spherical earth with a three-dimensional viscosity—I. Theory, *Geophys. J. Int.* **137,** 469–488.

Martinec, Z., Matyska, C., Čadek, O. & Hrdina, P., 1993. The Stokes problem with 3-D Newtonian viscosity in a spherical shell, *Comput. Phys. Commun.*, **76,** 63–79.

Martinec, Z., Čadek, O. & Fleitout, L., 2001. Can the 1-D viscosity profiles inferred from postglacial rebound data be affected by lateral viscosity variations in the tectosphere? *Geophys. Res. Lett.*, **28,** 4403–4406.

Masters, G., Johnson, S., Laske, G. & Bolton, H., 1996. A shear-velocity model of the mantle, *Phil. Trans. R. Soc. Lond.,* A, **345,** 1385–1411.

Montagner, J.-P. & Tanimoto, T., 1991. Global upper mantle tomography of seismic velocities and anisotropies, *J. geophys. Res.*, **96,** 20 337–20 351.

Nataf, H.-C. & Ricard, Y., 1996. 3SMAC: an *a priori* tomographic model of the upper mantle based on geophysical modeling, *Phys. Earth planet. Inter.*, **95,** 101–122.

Panasyuk, S.V. & Hager, B.H., 2000. Models of isostatic and dynamic topography, geoid anomalies, and their uncertainties, *J. geophys. Res.*, **105,** 28 199–28 209.

Peltier, W.R., 1989. Mantle viscosity, in *Encyclopedia of Solid Earth Geophysics,* ed., James, D.E., Van Nostrand Reinhold, New York.

Peltier, W.R. & Jiang, X., 1996. Glacial isostatic adjustment and Earth rotation: refined constraints on the viscosity of the deepest mantle, *J. geophys. Res.*, **101,** 3269–3290.

Peltier, W.R., Forte, A.M., Mitrovica, J.X. & Dziewonski, A.M., 1992. Earth's gravitational field: seismic tomography resolves the enigma of the Laurentian anomaly, *Geophys. Res. Lett.*, **19,** 1555–1558.

Press, V.H., Teukolsky, S.A., Wetterling, W.T. & Flannery, B.P., 1992. *Numerical Recipes in Fortran. The Art of Scientific Computing*, Cambridge University Press, Cambridge.

Ravine, M.A. & Phipps Morgan, J., 1993. Geoid effects of lateral viscosity variations near the top of the mantle: a 2-D model, *Earth planet. Sci. Lett.*, **119,** 617–625.

Ribe, N.M., 1992. The dynamics of thin shells with variable viscosity and the origin of toroidal flow in the mantle, *Geophys. J. Int.* **110,** 537–552.

Ricard, Y. & Bai, W., 1991. Inferring viscosity and the 3-D density structure of the mantle from geoid, topography and plate velocities, *Geophys. J. Int.* **105,** 561–572.

Ricard, Y. & Vigny, C., 1989. Mantle dynamics with induced plate tectonics, *J. geophys. Res.*, **94**, 17 543–17 560.

Ricard, Y., Fleitout, L. & Froidevaux, C., 1984. Geoid heights and lithospheric stresses for a dynamic Earth, *Ann. Geophys.*, **2,** 267–286.

Ricard, Y., Froidevaux, C. & Fleitout, L., 1988. Global plate motion and the geoid: a physical model, *Geophys. J.*, **93,** 477–484.

Ricard, Y., Doglioni, C. & Sabadini, R., 1991. Differential rotation between lithosphere and mantle: a consequence of lateral mantle viscosity variations, *J. geophys. Res.*, **96,** 8407–8415.

Richards, M.A. & Hager, B.H., 1989. Effects of lateral viscosity variations on long-wavelength geoid anomalies and topography, *J. geophys. Res.*, **94,** 10 299–10 313.

Ringwood, A.E., 1990. Slab–mantle interactions, 3, Petrogenesis of intraplate magmas and structure of the upper mantle, *Chem. Geol.*, **82,** 187–207.

Ritzert, M. & Jacoby, W.R., 1992. Geoid effects in a convecting system with lateral viscosity variations, *Geophys. Res. Lett.*, **19,** 1547–1550.

Sclater, J.G., Jaupart, C. & Galson, D., 1980. The heat flow through oceanic and continental crust and the heat loss of the Earth, *Rev. Geophys. Space Phys.*, **18,** 269–311.

Solomatov, V.S. & Stevenson, D.J., 1994. Can sharp seismic discontinuities be caused by non equilibrium phase transformations?, *Earth planet. Sci. Lett.*, **125,** 267–279.

Steinberger, B. & O'Connell, R.J., 1998. Advection of plumes in mantle flow: implication for hotspot motion, mantle viscosity and plume distribution, *Geophys. J. Int.* **132,** 412–434.

Stevenson, D.J., 1997. Temperature–dependent phase assemblages and the interpretation of seismic tomography (abstract), *EOS, Trans. Am. geophys. Un.*, **78**, Fall Meet. Suppl., F466.

Su, W.-J., Woodward, R.L. & Dziewonski, A.M., 1994. Degree 12 model of shear velocity heterogeneity in the mantle, *J. geophys. Res.*, **99,** 6945–6980.

Thoraval, C., Machetel, P. & Cazanave, A., 1995. Locally layered convection inferred from dynamic models of the Earth's mantle, *Nature*, **375,** 777–780.

Thoraval, C. & Richards, M.A., 1997. The geoid constraint in global geodynamics: viscosity structure, mantle heterogeneity models and boundary conditions, *Geophys. J. Int.* **131,** 1–8.

Tromp, J. & Mitrovica, J.X., 1999. Surface loading of a viscoelastic earth—I. General theory, *Geophys. J. Int.* **137,** 847–855.

van der Hilst, R.D., Widiyantoro, S. & Engdahl, E.R., 1997. Evidence for deep mantle circulation from global tomography, *Nature*, **386,** 578–584.

Weidner, D.J. & Wang, Y., 2000. Phase transformations: implications for mantle structure, in *Earth's Interior*, pp. 215–235, Geophysical monograph 117, AGU, 2000.

Wen, L. & Anderson, D.L., 1997. Present-day plate motion constraint on mantle rheology and convection, *J. geophys. Res.*, **102,** 24 639–24 653.

Woodhouse, J.H. & Trampert, J., 1995. Global upper mantle structure inferred from surface wave and body wave data (abstract), *EOS, Trans. Am. geophys. Un.*, **76,** Fall Meet. Suppl., F422.

Zhang, S., 1993. 3-D modeling of present mantle structure, constrained by plate subduction, geoid and mantle tomography: flow in a spherical shell with lateral viscosity variations, *PhD thesis*, University of Mainz, Mainz, Germany.

Zhang, S. & Christensen, U.R., 1993. Some effects of lateral viscosity variations on geoid and surface velocities induced by density anomalies in the mantle, *Geophys. J. Int.* **114,** 531–547.

Zhong, S. & Davies, G.F., 1999. Effects of plate and slab viscosities on the geoid, *Earth planet. Sci. Lett.*, **170,** 487–496.

Zhong, S. & Gurnis, M., 1996. Interaction of weak faults and non-Newtonian rheology produces plate tectonics in a 3-D model of mantle flow, *Nature*, **383,** 245–247.